J. Fluid Mech. (1986), *vol.* 172, *pp.* 453–480
Printed in Great Britain

Measurements of internal gravity waves in a continuously stratified shear flow

By C. GARY KOOP AND BRIAN McGEE
TRW Space and Technology Group, Redondo Beach, CA 90278, USA

(Received 27 June 1983 and in revised form 13 May 1986)

A theoretical wave-action model, based on the work of Grimshaw (1974), is presented which describes broadbanded internal wave motions in a stratified shear flow with the viscous terms included. The model shows that in the neighbourhood of the critical level viscosity can have important effects and can stabilize the flow with respect to convective overturning. The predictions of the model are compared with the results of an experimental study where detailed measurements of the velocity and density fields are made within an internal wave packet propagating through a continuously stratified shear flow. The results show that the model accurately predicts the occurrence or non-occurrence of wave overturning due to interactions with the shear, and provides an accurate description of the structure of the wave-induced density and velocity fluctuations in those regions of the flow where the assumptions of the model are satisfied.

1. Introduction

In a previous paper (Koop 1981) we presented preliminary results pertaining to the propagation of internal gravity waves in a stratified shear flow. The results of that work were primarily qualitative and presented in the form of shadowgraph visualizations. The intent of the present study is to expand upon our previous work and investigate the phenomenology of wave/shear interactions in a more quantitative manner. Toward this goal, we have instrumented the experimental facility with a number of flow sensors, primarily hot-film gauges and conductivity probes, so that a detailed description of the wave field velocity and density structure may be obtained.

Of particular concern in this study is the characterization of wave/shear interactions which lead to the production of localized turbulent events. Such wave-induced turbulent mixing can have an important effect upon vertical diffusion processes in both the atmosphere and ocean (cf. Bell 1975; Munk 1980). To interpret the experimental results, we have appealed to the theory of wave-action density, as derived by Bretherton (1966), Grimshaw (1974), Broutman (1982), among others. In presenting the experimental results, a number of direct comparisons are made between the predictions of this theory and the measurements. The experiments presented compliment those of Thorpe (1981) who considered sinusoidal waves in an accelerating flow, and include broadband disturbances generated by compact sources in addition to sinusoidal waves in a steady stratified shear flow. The analytical method utilized differs from Thorpe's perturbation approach in that the WKB approximation is employed in a wave-action formulation.

2. Theoretical background

An important contribution made to the understanding of internal gravity waves propagating in a moving fluid was made by Bretherton (1966). Using the WKB approximation, Bretherton considered the interaction of small amplitude waves with an inviscid slowly varying shear flow. The essential result of this work was the derivation of a conservation equation describing the evolution of the wave-action density; a quantity which represents the local energy density divided by the intrinsic frequency of the wave. An extension to this analysis was made by Grimshaw (1974) who removed the small amplitude assumption and included the effects of dissipation and thermal diffusion to derive the following set of equations (nomenclature is that of Grimshaw 1974):

$$A_t + \nabla\cdot[A(\boldsymbol{c}+\boldsymbol{U})] + \nu\kappa^2(\boldsymbol{x})\,A = 0, \tag{1}$$

$$\rho_0 \frac{\mathrm{D}U}{\mathrm{D}t} + \nabla\cdot[Ac\boldsymbol{\kappa}_{\mathrm{H}}] + \nabla_{\mathrm{H}}\,p = 0. \tag{2}$$

Equations (1) and (2) are fully nonlinear with no restrictions being made on wave amplitude. As a result, the equations are inextricably coupled, with mean flow modifications being driven by gradients in wave action which subsequently feed back into the wave-action equation. As noted by Grimshaw (1975), however, in the small-amplitude limit this feedback process is removed and the two equations become decoupled such that the mean flow does not vary in time.

A further simplification to this system of equations can be made by assuming the wave field to be stationary in time (i.e. lee waves). For the purposes of the present investigation this simplification is appropriate, as lee-wave generation is the experimental technique employed for the production of internal waves. For small-amplitude stationary lee waves, a two-dimensional sinusoidal disturbance of horizontal wavenumber k in a steady shear flow (for infinite Prandtl number) is prescribed by the following

$$\frac{\partial}{\partial z}(c_{zk}\,A_k) + \nu[k^2 + n_k^2(z)]\,A_k = 0, \tag{3}$$

where

$$A_k = \tfrac{1}{2}\rho_0 \frac{N^2 w_k^2(z)}{\omega_k'^3}. \tag{4}$$

Here, $w_k(z)$ is related to the two-dimensional wave-induced vertical velocity field $w_k(x,z)$ for wavenumber k as:

$$w_k(x,z) = w_k(z)\exp(\mathrm{i}kx) + \text{complex conjugate}. \tag{5}$$

Assuming conditions to be known at some level, $z = z_0$, (3) may be integrated to yield:

$$A_k(z) = A_k(z_0)\frac{c_{zk}(z_0)}{c_{zk}(z)}\left\{\int_{z_0}^{z} \exp\left[-\nu\frac{k^2+n_k^2(z')}{c_{zk}(z')}\right]\mathrm{d}z'\right\}. \tag{6}$$

For spatially compact disturbances comprised of many horizontal wavenumbers, Fourier superposition techniques are employed. In this case, the wave-induced density and velocity fields may be computed from $w(x,z)$ as:

$$\rho(x,z) = \frac{N^2(z)\,\rho(z)}{gU(z)}\sum_k \frac{w_k(z)}{\mathrm{i}k}\exp\left\{\mathrm{i}\left[kx + \int_{z_0}^{z} n_k(z')\,\mathrm{d}z'\right]\right\} + \text{c.c.} \tag{7a}$$

$$u(x,z) = -\sum_k \frac{n_k(z)}{k}\,w_k(z)\exp\left\{\mathrm{i}\left[kx + \int_{z_0}^{z} n_k(z')\,\mathrm{d}z'\right]\right\} + \text{c.c.} \tag{7b}$$

Equations (3)–(7) constitute the analytic model used to compare wave-action analysis with the results of the experimental investigation. As presently formulated, the analysis is more restrictive than Grimshaw's original derivation. The assumptions inherent in the present analytic model are:

(*a*) The medium is slowly varying such that the parameter

$$\epsilon = \frac{N^2 L}{g} \ll 1;$$

(*b*) The disturbances are weak (i.e. $ka \ll 1$ where a is the disturbance amplitude) in order to decouple the wave action and mean flow equations;

(*c*) The waves are stationary lee waves;

(*d*) The infinite Prandtl number limit has been taken.

In §5, the accuracy of these assumptions as applied to the description of the present experimental results are discussed.

3. Experimental apparatus and procedure

The experimental facility shown in figure 1 (*a*) is the same as that described fully in Koop (1981). The channel is stratified in a continuous fashion by smoothly varying the salinity content of the fluid from bottom to top. The fluid moves around the annular channel under the action of the pumping mechanism, depicted in figure 1 (*b*), which consists of two stacks of closely spaced circular plates that counter-rotate and impart momentum to the fluid by viscous stresses. A double gearing system permits independent control of the rotation rate of the upper and lower halves of the two stacks, and differential rotation between the two halves is used to produce a shearing motion.

Internal waves are generated by towing several types of solid objects through the test section in the same direction as the fluid motion. A shadowgraph system is used to visualize the resulting wave field. Figure 2 shows the manner in which wave fields containing a critical level are generated. For towing speeds less than the maximum flow velocity, the internal lee waves radiating away from the solid object encounter a point in the flow where the local fluid velocity matches the wave propagation speed, which by definition is the location of the critical level. Two classes of disturbances were studied, viz. sinusoidally varying corrugated boundaries several wavelengths in spatial extent and spatially compact disturbances having contour shapes that were Gaussian profiles. Table 1 (*a*) summarizes the characteristics of these disturbance sources. Table 1 (*b*) summarizes the test conditions used. Typically the fluid velocity varied between nearly zero close to the bottom, and 3–5.5 cm/s in the upper region of the channel. Over this range of velocities, the ambient gradient Richardson number, Ri, within the sheared region varied between 5 and 50.

An addition made to the original experimental apparatus of Koop (1981) is a sensor system used for making quantitative measurements of both the velocity and density fields generated by the internal wave fields under study. This sensor system, shown schematically in figure 3, consists of:

(*a*) An 11-sensor vertically aligned rake of conductivity probes fixed in laboratory coordinates;

(*b*) A 10-sensor vertically aligned rake of hot-film anemometers fixed in laboratory coordinates;

(*c*) A 3-sensor hot-film, conductivity probe, thermistor arrangement which continuously cycled vertically up and down at a constant speed (± 1.65 cm/s). The fixed

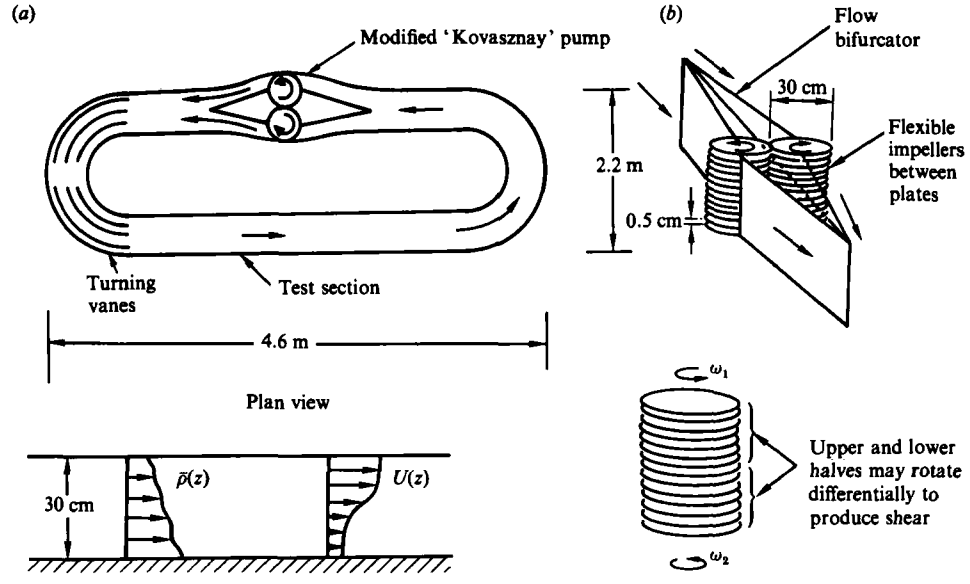

FIGURE 1. (*a*) Schematic of the stratified shear-flow facility. (*b*) Detail of the pumping mechanisms.

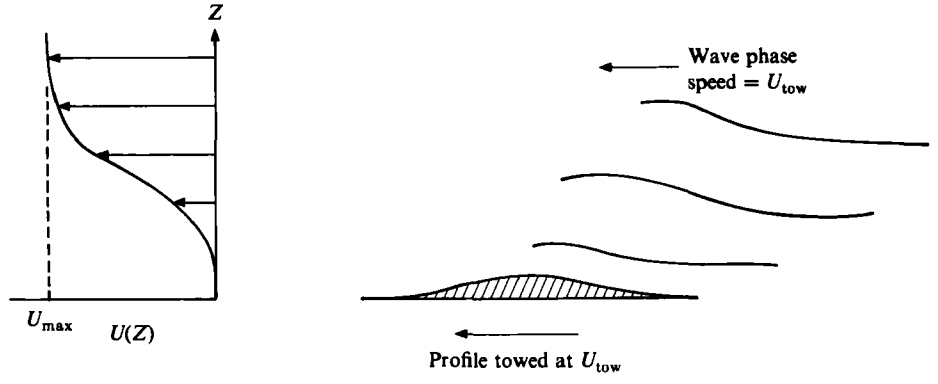

FIGURE 2. Sketch depicting manner in which critical layer flows were generated experimentally. For critical layer operation: $U_{tow} < U_{max}$.

sensors are laterally offset from the cycling probes to prevent their being influenced by the motion of the oscillating probes.

The fixed-rake probes provide a quantitative measure of the time history of the velocity and density fields at several discrete vertical positions as the waves propagate past the sensors. The cycling probes measure the vertical structure of the flow field. Figure 4 presents an example of the mean velocity distribution measured using the vertically cycling anemometer. The velocity distribution measured simultaneously by recording the distortion of a vertical dye streak is presented for comparison.

(*a*)

I. Corrugated wall 1: $\lambda = 7.5$ cm; a (peak-trough) = 0.48 cm; Total length = 90 cm

II. Corrugated wall 2: $\lambda = 15$ cm; a (peak-trough) = 0.96 cm; Total length = 90 cm

III. Gaussian profile 1: $a_0 = 0.5$ cm, $\lambda = 7.5$ cm

IV. Gaussian profile 2: $a_0 = 1$ cm, $\lambda = 7.5$ cm

$$a(x) = a_0 \exp\left[-\left(\frac{x}{\lambda}\right)^2\right]$$

(*b*)

Test condition	Internal wave source	Towing speed (cm/s)	$Ri_0 = N^2/(U_z)^2$	Maximum fluid speed (nominal) (cm/s)	Description
I*a*	$\lambda = 7.5$ cm Corrugated wall	2.5	40–50	3.1	Stable critical layer monochromatic forcing
I*b*	$\lambda = 15$ cm Corrugated wall	3.88	4	5.7	Unstable critical layer, monochromatic forcing
II	$a_0 = 0.5$ cm Gaussian profile 1	3.88	40–50	3.5	Stable IW/Shear interaction with no critical layer within vertical aperture of probe array
III	$a_0 = 1$ cm Gaussian profile 2	3.88	40–50	3.5	Unstable IW/Shear interaction with no critical layer within vertical aperture of probe array
IV	$a_0 = 0.5$ cm Gaussian profile 1	3.88	5	5.5	Unstable IW/Shear interaction with critical layer
V	$a_0 = 1$ cm Gaussian profile 2	2.05	40–50	3.5	Stable IW/Shear interaction with critical layer

TABLE 1. (*a*) Internal wave sources. (*b*) Experimental test conditions

4. Experimental results and comparison with theory

4.1. *Experiment I: corrugated wall experiments*

The first set of experiments to be discussed involves the wave field generated by a sinusoidally varying corrugated wall. As identified in table 1 (*a*), two such sources were utilized having wavelengths of 7.5 and 15 cm, respectively, and 90 cm in length.

Figure 5 shows the wave field (visualized using a shadowgraph) generated using the 7.5 cm corrugated boundary. In the photograph, the corrugated wall is positioned close to the bottom and is moving from right to left at a speed of 2.5 cm/s. The fluid

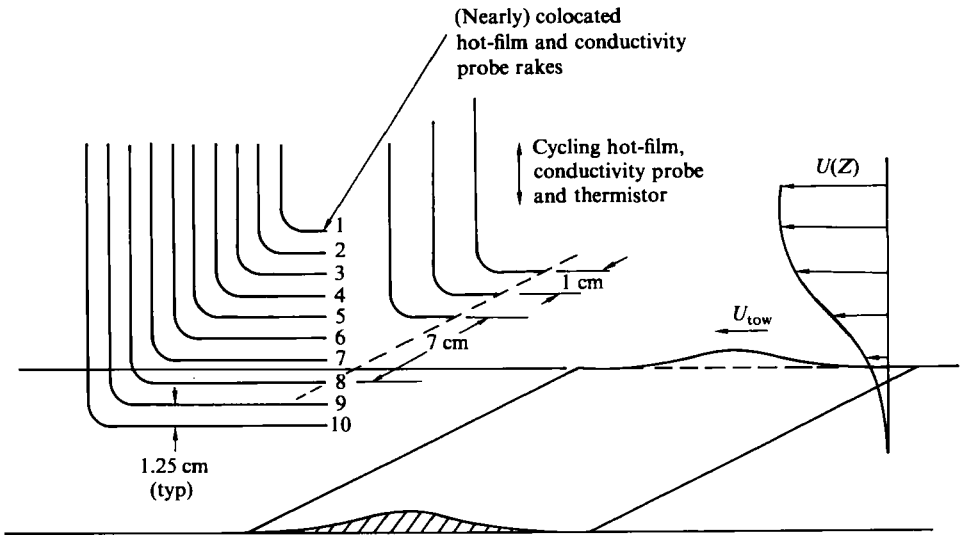

FIGURE 3. Schematic representation of probe system.

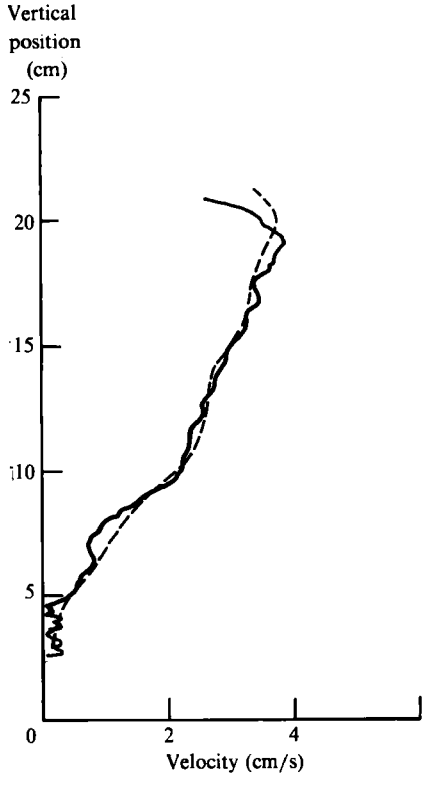

FIGURE 4. Velocity profile measurement (in laboratory-fixed coordinates) using cycling hot-film probe (——) compared with that deduced using the dye-line distortion technique (– – – –).

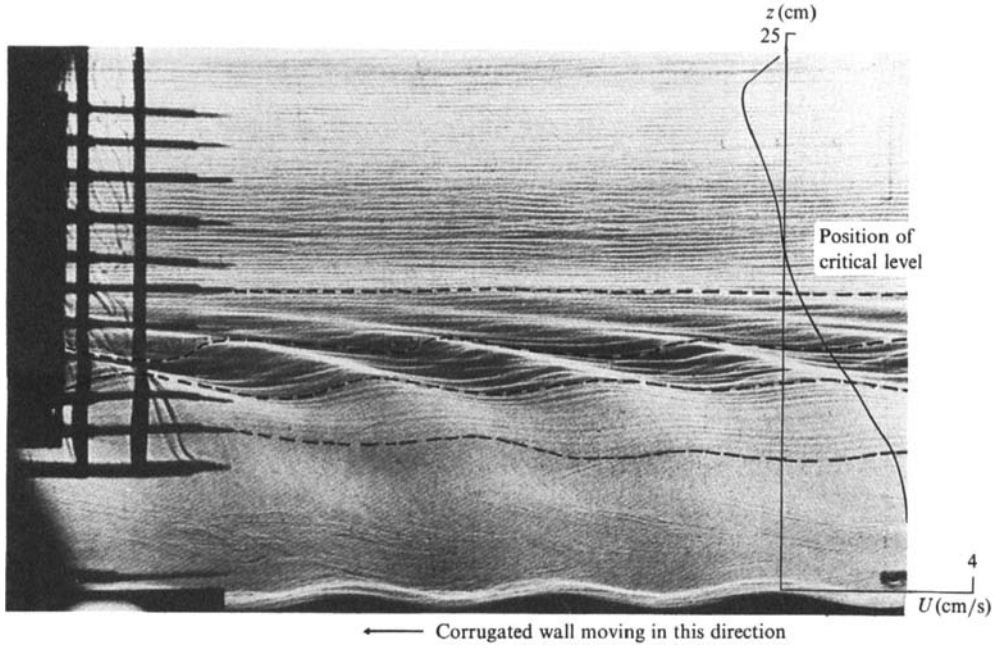

FIGURE 5. Shadowgraph image of wave field generated by 7.5 cm corrugated wall towed at 2.5 cm/s. Measured velocity profile (in coordinate system moving with corrugated wall) is shown superimposed on the photograph. Position of critical level noted by an arrow. Dotted lines have been superimposed on the photograph to accentuate the isopycnal displacements.

near the top is also moving right to left at a velocity of about 3.6 cm/s, while the fluid close to the bottom is nearly quiescent. The horizontal striations that appear in the upper half of the tank are due to small-scale mixing which occurs in a honeycomb flow straightener (not shown) located upstream. The presence of these striations proved useful in visualizing isopycnic displacements while having no observable influence upon the dynamics of the flow. The ambient velocity profile (in convected coordinates moving with the towing speed) is shown superimposed on the photograph. In this coordinate system, the critical layer is located at the point where the velocity is zero. The gradient Richardson number in the vicinity of the critical level is approximately 50.

From the wave field shown in figure 5, the inhibiting effect that the critical layer has upon the vertical propagation of the waves is clearly seen. Virtually no evidence of wave motion is observed in the upper half of the tank above the critical level. In the lower half of the channel, the wave displacements become significantly larger as the critical level is approached, but very close to the critical level the displacement amplitude diminishes to zero. Within the region where the displacement field is being amplified there also appears to be some asymmetry in the horizontal direction, with noticeably steeper wave slopes occurring on the forward face of the waves followed by more gradual slopes on the rear of the wave. Note that the flow in the neighbourhood of the critical level does not exhibit evidence of convective overturning or turbulence generation.

The theoretical displacement field calculated using the wave-action model discussed in §2 is shown in figure 6. For these calculations, the measured ambient velocity and density profiles were used in the model to compute the perturbed velocity field which

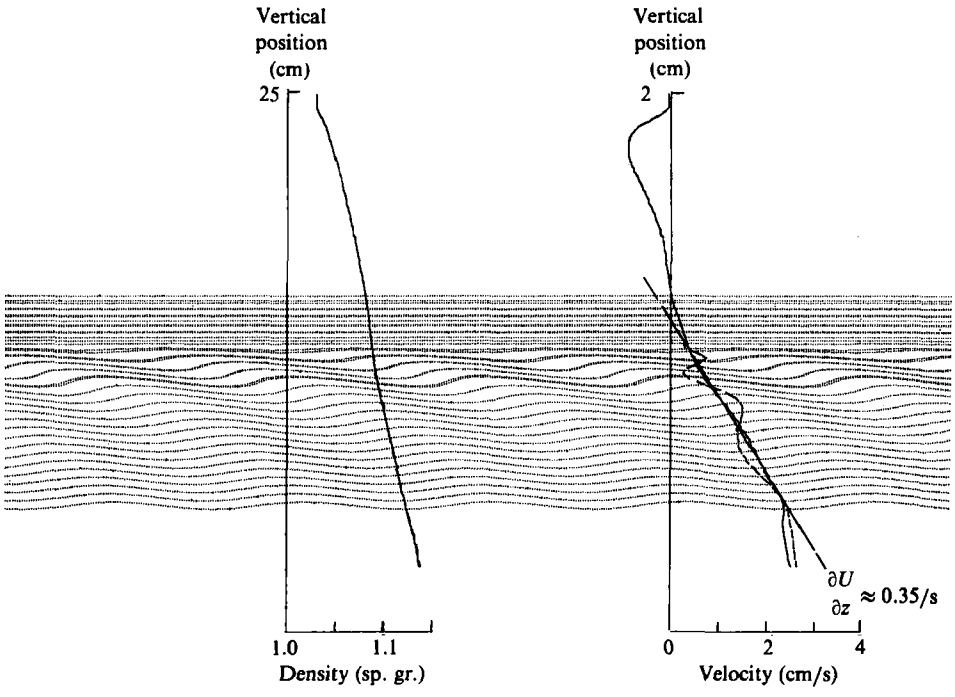

FIGURE 6. Displacement field computed for test conditions of figure 5. ——, ambient profile; – – – –, perturbed profile.

was subsequently integrated to compute streamlines. Since the infinite Prandtl number limit is taken in the model, for this steady-flow calculation streamline displacements are identical with isopycnic displacements. In comparing the theoretically computed displacements with the observations it is found that most of the features of the experiment are reproduced by the model. The tendency for waves to be amplified as they approach the critical level is clearly exhibited in the model, as well as the attenuation to zero amplitude at the critical-level position. The tendency for the forward face of the waves to become steeper as they approach the critical level is also noted in the calculations. Finally, the model does not predict overturning waves anywhere in the flow field (particularly near the critical level), which is consistent with the lack of turbulence observed in the experiment.

Also shown in figure 5 are the computed velocity and density profiles, which have been perturbed by the presence of the wave fields, superimposed upon the ambient distributions. The wave-induced density perturbations for this case are quite small, and not readily observed on the plot. The velocity perturbations are more readily seen. Note that the perturbed velocity field does not exhibit a zero crossing below the critical level. Orlanski & Bryan (1969) have argued that the occurrence of a zero crossing in the perturbed velocity field (in this convected coordinate system) must be accompanied by a region of negative density gradient. Such a negative gradient, unless balanced by viscous or diffusive effects or by centrifugal accelerations, would be statically unstable. Such static instability would lead to overturning and the production of turbulence, much like that occurring in breaking surface waves. That no such zero crossings are predicted for the perturbed velocity field is consistent with the lack of turbulent motions observed in the experimental data.

An example of a wave/shear interaction where turbulence generation is observed

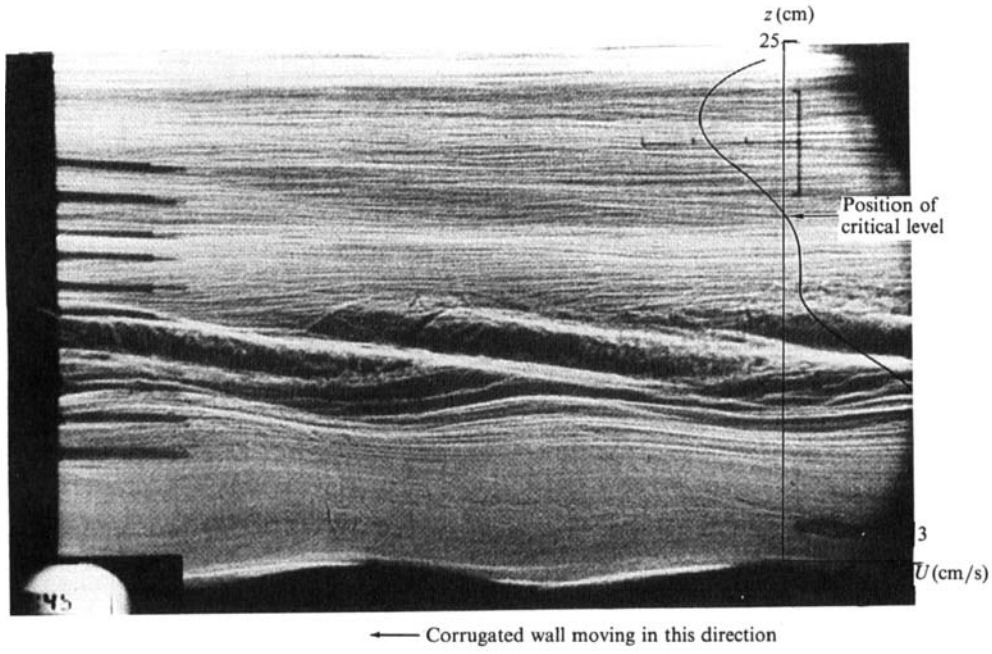

FIGURE 7. Shadowgraph of wave field generated by 15 cm corrugated wall towed at 3.88 cm/s. Measured velocity profile (in coordinate system moving with corrugated wall) is shown superimposed on the photograph. Position of critical level noted by an arrow.

at the critical level is shown in figure 7. Here the longer wavelength (15 cm *vs.* 7.5 cm) corrugated wall was used, and both the towing speed and the maximum fluid velocity were increased (table 1*b*). The results shown in this figure exhibit the same trapping effect upon vertical propagation above the critical level seen in the previous experiment (figure 5). Similarly, the tendency for wave displacements to grow as waves approach the critical level from below is exhibited in the figure. The primary difference between the experimental resuts shown in figure 7 and the previous data of figure 5 is the preponderance of turbulent motions in the region below the critical level.

The computed displacement field for this test condition is shown in figure 8. The calculations clearly exhibit overturning waves in the region in which turbulence is observed in the photograph. The implication is that as the waves approach the critical level they become convectively unstable and this leads to turbulence production as the overturning process develops statically unstable density gradients. This interpretation is supported by the computation of the perturbed velocity and density profiles where zero crossings in the velocity distribution correspond with regions of negative density gradient providing sites for convective instability, consistent with the aforementioned theory of Orlanski & Bryan (1969). The details of the wave/shear interaction in the neighbourhood of the overturning waves and the subsequent generation of turbulence arising from the static instability are not describable by the wave-action model. However, the comparison of the calculations and observations in figures 5–8 suggests that the parametric boundary separating laminar interactions from incipient wave breaking and development of turbulent motions may be predicted by the model. This transition from laminar to turbulent wave/shear interactions is believed to be due to changes in the relative importance

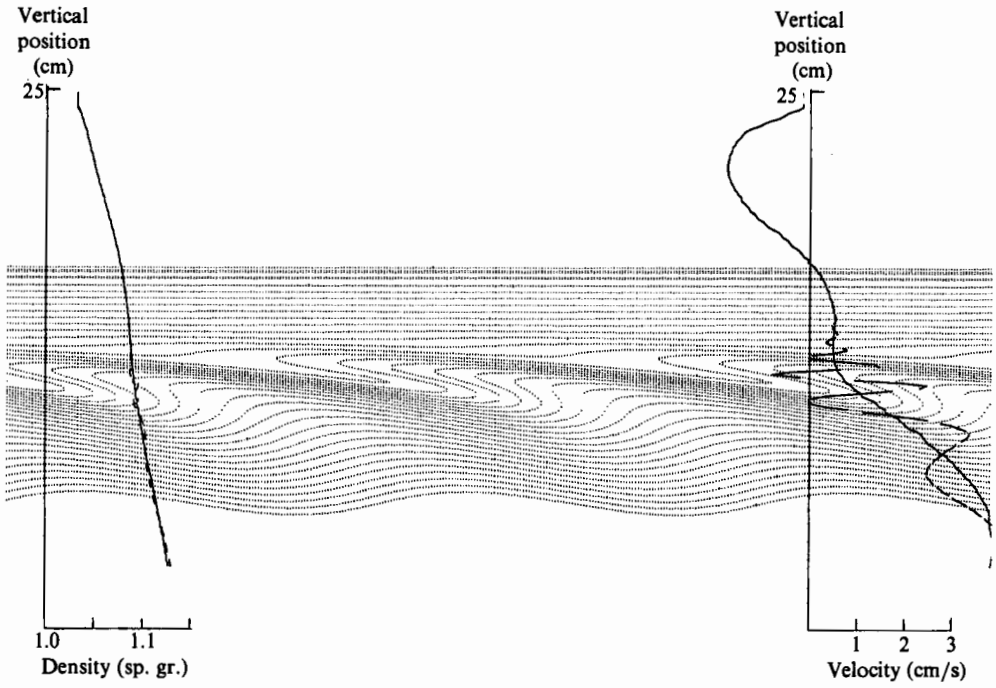

FIGURE 8. Displacement field computed for the test conditions of figure 7. ——, ambient profile; – – – –, perturbed profile.

of viscous effects upon the dynamics of the wave field. For example, if viscosity is zero the wave-action model predicts wave overturning at some point in the flow for all internal wave/critical-level flows (at positions progressively closer to the critical level as the viscosity is decreased). For finite viscosity, however, viscous effects act to impede this overturning process, and whether or not overturning occurs is dependent upon a number of parameters including the local Richardson number, the wavenumber, and the vertical wave-action flux. Koop (1981) presents a simple criterion based on a piecewise linear velocity profile which determines the conditions under which viscous stresses are sufficient to suppress the natural tendency of waves to overturn near the critical level. Approximating the measured velocity profiles in the present experiments by straight line segments and applying this criterion correctly predicts the stability (i.e. no wave overturning) for the wave field shown in figure 5, and instability (wave overturning) for that shown in figure 7 (see Appendix A for details).

4.2. *Experiment II: Gaussian profile, non-critical flow*

To examine the effects of shear on spatially compact non-sinusoidal disturbances a series of experiments was performed using a simple Gaussian profile shape as the internal wave source. Table 1 summarizes the experimental test conditions and the characteristics of the particular profile used for experiment II. For this test, the fluid velocity (in laboratory-fixed coordinates) varies between 0.1 cm/s near the bottom to a maximum of 3.95 cm/s near the top. The mean flow Richardson number is approximately 50 ($\pm 10\%$). The towing speed of the Gaussian profile is 3.88 cm/s. For these experiments the full diagnostic probe arrays (both fixed and vertically

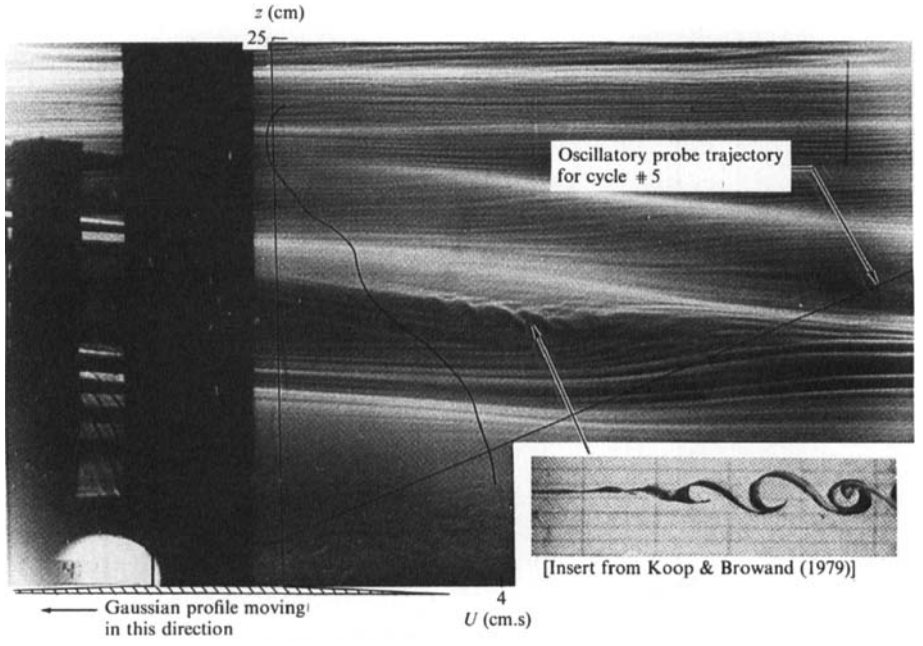

FIGURE 9. Shadowgraph image of wave field generated by Gaussian profile 1 for test condition II. Insert is an example of a Kelvin–Helmholtz instability reproduced from Koop & Browand (1979). Note similarity between Kelvin–Helmholtz waves and those observed in the central portion of the photograph. Measured velocity profile (in coordinate system moving with the towed body) superimposed on the photograph shows a critical layer existed outside the vertical aperture of the instrumented portion of the flow field.

cycling) were employed. Since the towing speed is smaller than the maximum fluid velocity, a critical level exists in the flow. It is noted, however, that the position of the critical level is 2 cm above the uppermost probe in the diagnostic array, and consequently is outside the vertical aperture of the instrumented portion of the flow field. Within the aperture of the instruments a critical level does not exist.

The shadowgraph image of the wave field for experiment II is shown in figure 9. In the photograph, the Gaussian profile generating the waves (which was out of the field of view of the camera) is shown drawn to scale in the lower portion of the figure. The profile is being towed from right to left, and the measured velocity profile (in coordinates moving with the towed obstacle) is also shown. The vertically aligned sensor array is partially seen in the extreme left-hand side of the photograph. Several distinct features exist in the photograph including the appearance of two bright bands inclined at an angle of approximately 10° with respect to the horizontal indicating a region of intense curvature in the density profile. It is also noted that the wave field is almost devoid of turbulent motions, with the possible exception of a curious wavelike structure observed in the centre of the photograph. The visual appearance of these waves is very similar to that of turbulent billows which evolve from the growth of a Kelvin–Helmholtz instability, an example of which is shown as an insert in figure 9, reproduced from Koop & Browand (1979). Whether such an instability is anticipated on the basis of local Richardson number considerations may be examined from the velocity and density profile measurements. Figure 10 shows the density profile measured by the cycling conductivity probe measured prior to the

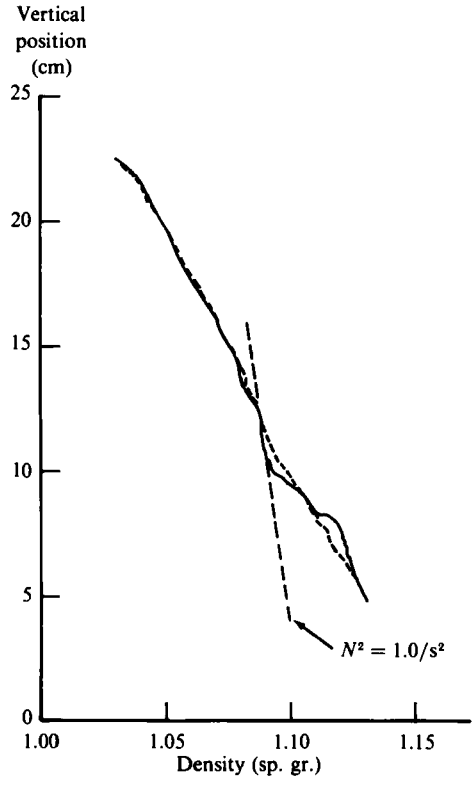

FIGURE 10. Measured density profiles along ----, cycle 1 (ambient flow prior to the arrival of the waves) and ——, cycle 5 (within the wave field) for test condition II.

arrival of the wave field (cycle 1) and within the wave field generated by the towed Gaussian-shaped object (cycle 5). The corresponding velocity profiles measured on cycles 1 and 5 of the vertically cycling probes (in a coordinate system moving with the towed Gaussian profile) are shown in figure 11 (for reference, the vertical positions occupied by the fixed rake sensors are also shown in this figure). From these profiles, the ambient flow gradient Richardson number is measured to be approximately 50. Locally within the wave field, however, the wave-induced velocity and density perturbations produce a Richardson number which is significantly smaller, approximately 0.2, suggesting that the wavelike structure observed in figure 9 was generated as a result of a dynamical Kelvin–Helmholtz instability in the region where the internal wave field generated by the towed obstacle interacting with the shear flow locally produce a Richardson number smaller than the critical value of 0.25. It is to be pointed out here that the computed Richardson number distribution based on the wave-action model also exhibits localized regions where the Richardson number falls below the critical value necessary for the growth of the Kelvin–Helmholtz instability.

The density field measured by the conductivity sensors on the stationary vertically aligned probe array is shown in figure 12. The data presented represent density fluctuations recorded at eleven discrete vertical positions as a function of time as the waves propagate past the probes. In this density–time representation, a region of zero vertical gradient of density (i.e. the point of incipient wave overturning) is represented by a coalescence of two or more density traces, such that at a particular point in time

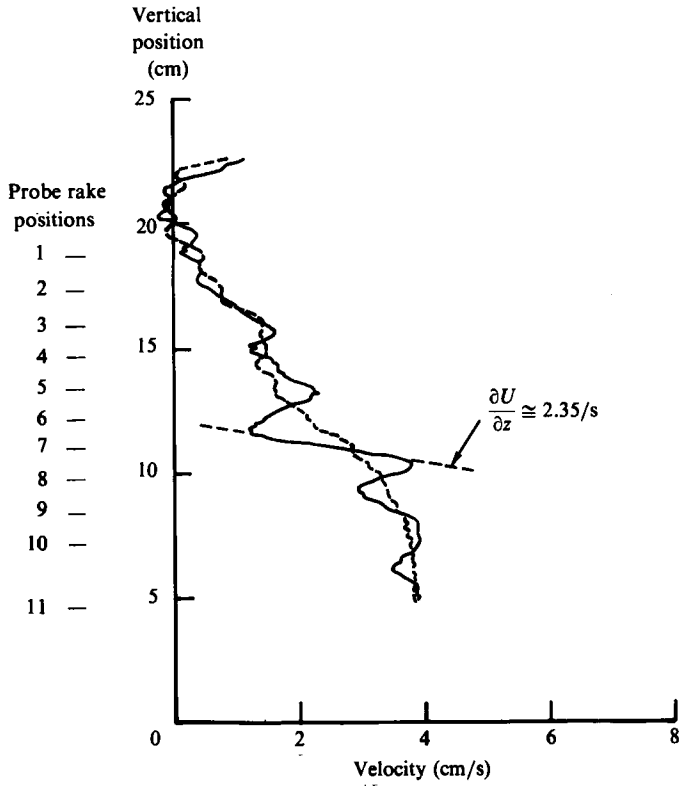

FIGURE 11. Measured velocity profiles along trajectories of ----, cycle 1 and —— cycle 5 for test condition II.

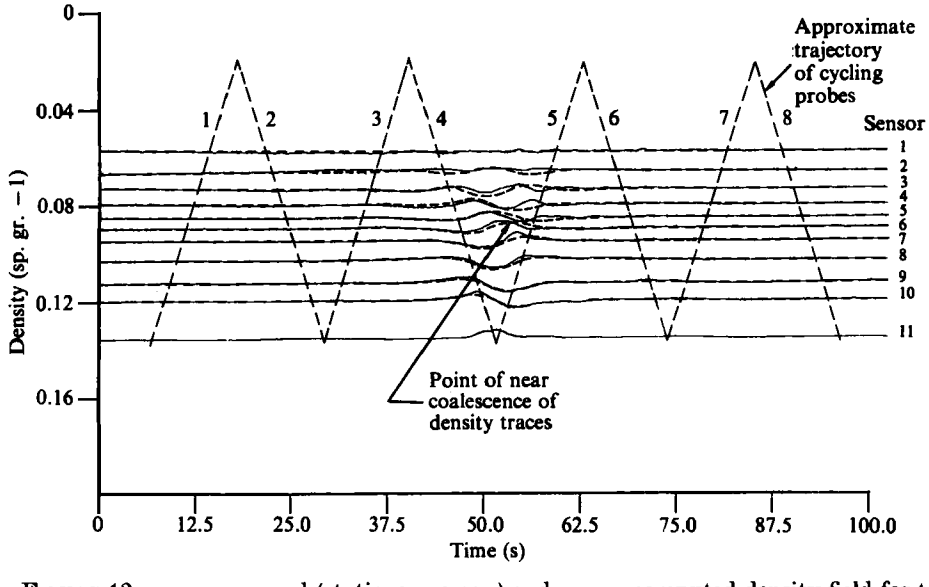

FIGURE 12. ——, measured (stationary array) and ----, computed density field for test condition II.

two probes vertically separated encountered fluid of the same density. Wave overturning, characterized by regions of negative density gradient are identified by density traces which cross over one another. One would anticipate such an overturning event to generate turbulence, such that at times following the intersection of two density traces high-frequency activity should be noted in the data. Also shown in figure 12 as dotted lines are the predictions of the wave-action model along with the approximate trajectory in density–time space which the vertically cycling probes followed during the experiment.

The data from sensor number 11 in figure 12, which was the lowermost sensor positioned 4.5 cm above the towed Gaussian internal wave source, show a density perturbation characterized by single pulse-like disturbance toward lower density corresponding to a downwelling of fluid. Above this position, the measurements show vertical mode structure exhibiting cyclic variations of upwelling and downwelling, but the amplitude of the measured fluctuations diminishes near the top of the array. Sensor number 1 exhibits virtually no evidence of the internal wave field generated by the towed Gaussian shaped object. Denoted by an arrow in figure 12 is a region of near coalescence of density traces, which, as previously pointed out, corresponds to regions of nearly vertical isopycnic displacement. The location of these nearly vertical contours corresponds with the position of the observed wavelike disturbances believed to be due to Kelvin–Helmholtz instability which are observed in figure 9. Within this region the simple structure of upwelling or downwelling becomes more complex as features with shorter lengthscales (presumably due to the Kelvin–Helmholtz waves) are being observed, particularly on sensors 3–7.

Figure 13 shows the corresponding velocity fluctuations measured by the vertically aligned array for experiment II, plotted in the coordinate system moving with the towed object. Also shown are the calculations from the wave-action model. The data from sensor 10 show a pulse-like disturbance with deceleration followed by acceleration of the fluid. For linear internal waves $u \sim -\partial\rho/\partial z$, so that this velocity data is consistent with the corresponding downwelling followed by upwelling pattern observed in the density measurement from sensor 10 in figure 12. Above this point, the data show vertical mode structure with cyclic variations in velocity perturbations analogous to that observed in the density data. Near the top of the sensor array, the disturbance amplitude becomes attenuated, and sensor 1 shows virtually no evidence of internal wave motion. For several of the probes, viz. 3, 4, and 5, the perturbed velocity traces exhibit points of near-zero velocity. The location of these near-zero crossings closely corresponds to the near coalescence of density traces in figure 12. Such correspondence is to be expected on the basis of the previously discussed model of Orlanski & Bryan (1969). Within the region where Kelvin–Helmholtz waves are observed in the shadowgraph pattern (noted in the figure) the character of the wave field changes, with shorter-scale structures being observed, similar to those found in the density traces.

The data presented in figures 10–13 provide a basis for comparing the wave-action model discussed in §2 with measurements of internal waves in a sheared environment. Superimposed on the measurements in figure 12 is the theoretical density field, computed using the measured ambient velocity and density profiles of figures 10 and 11. The measurements from sensor 11 in the conductivity probe array are used to initialize the model. In comparing the predictions with the experimental results it is found that many of the important features of the data are reproduced by the model. For example, the vertical mode structure of downwelling followed by upwelling on sensors 9 and 10 are predicted by the model to an accuracy of about 5%. On sensors

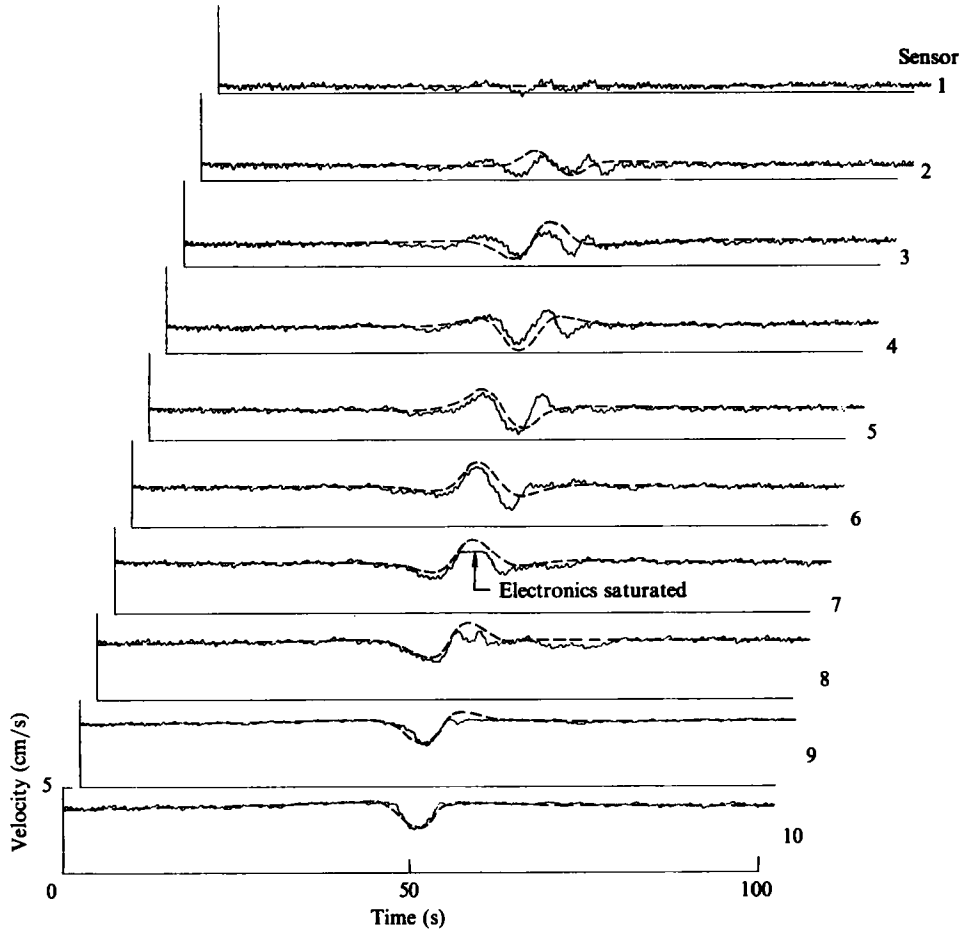

FIGURE 13. ——, measured (stationary array) and – – – –, computed velocity field for test condition II.

6–8 the character of the computed wave field changes to upwelling followed by downwelling, similar to what is observed in the data. For these sensors, the upwelling portion of the wave field is well predicted by the model (to within about 10%) but the downwelling portion shows poor agreement with the data. This is not unexpected, however, since this is the region where Kelvin–Helmholtz waves are observed in the shadowgraph image of figure 9. Clearly, the shorter-scale disturbances due to Kelvin–Helmholtz waves observed in the data are not reproduced by the model since such dynamical instabilities are not incorporated in the model. In the region of the flow where such dynamical waves are absent, however, the agreement with the data is generally to within about 10–20%. Note too, that close to the top of the array (sensor 1) both the theory and the experiment show a marked attenuation in the disturbance amplitude. Recalling the previous discussion of figure 6 regarding the attenuating effect of viscosity near the critical level, and noting from figure 10 that sensor 1 is within about 2 cm of a critical level, it is concluded that the observed and predicted attenuation near the top of the array is due to the increasing *importance* of viscosity near the critical level.

The corresponding predictions of the velocity fluctuations for this experiment are

shown superimposed on the data of figure 13. The character of the data of sensor 10 with deceleration followed by acceleration is predicted by the model to about 5% accuracy. Above this, the vertical mode structure of acceleration and deceleration on the forward portion of the wave field for sensors 4–8 is well predicted by the model (about 10% accuracy), but the rear portion of the wave field shows significant deviations from the data. For sensors 2–5 this is most likely due to the aforementioned Kelvin–Helmholtz waves which superimpose shorter-scale disturbances upon the internal wave field produced by the towed Gaussian profile. As previously mentioned, such processes are not modelled in the wave-action theory. Finally, the attenuation of the disturbance amplitude noted in the density data is also predicted by the model for the velocity field.

4.3. *Experiment III: amplitude effects*

To investigate the effect of the amplitude of the internal wave source upon the character of the internal wave/shear interaction, the test conditions for experiment II were repeated using the larger amplitude Gaussian profile (1 cm amplitude *vs* 0.5 cm for experiment II). Both the towing speed and the flow conditions for this experiment were identical with those of experiment II.

Figure 14 shows the shadowgraph image of the wave field for this test condition. Perhaps the most striking feature of this visualization is the presence of a great deal of turbulent activity within a banded region inclined about 10° from the horizontal in the mid-depth region of the channel. The location of this turbulent activity closely coincides with the position where Kelvin–Helmholtz waves were observed in the previous experiment. All but the very lowest probe on the vertical sensor array (conductivity sensor 11) passed through this turbulent region. Above the turbulent region two bright lines of constant phase are observed also inclined at an angle of about 10° which do not exhibit evidence of largescale overturning and turbulence production (an example of an exceptionally energetic wave field which destabilized several constant phase lines is presented in Koop (1981), figure 12).

The measured vertical density profile for the experiment depicted in figure 14, obtained using the vertically cycling array, is presented in figure 15. Shown here is the ambient density profile (cycle 1) along with the profile perturbed by the internal wave field generated by the towed Gaussian-shaped obstacle (cycle 5). In the ambient flow, the density distribution is approximately linear. The perturbed profile is quite different, however, with a region of negative gradient observed 10 cm above the internal wave source which is in the region where turbulent activity is observed in the shadowgraph visualization.

The corresponding profile of velocity measured using the vertically cycling hot film is shown in figure 16 for both the ambient and perturbed fields. Note the large wave-induced perturbation which nearly produces a zero crossing in the velocity signal which, according to the Orlanski & Bryan (1969) model is indicative of wave overturning.

The density field measured for the experiment depicted in figure 14 using the conductivity array is shown in figure 17. Some of the data shown exhibit features similar to those observed for the smaller amplitude internal wave source (figure 12), with the exception that the magnitude of the perturbations is larger. For example, the vertical mode structure such as the downwelling observed on sensor 11 evolving into upwelling followed by downwelling on sensor 10 is similar to what is found in figure 12. Above this point, however, the initial portion of the wave field shows upwelling or downwelling well correlated with the internal waves generated by the

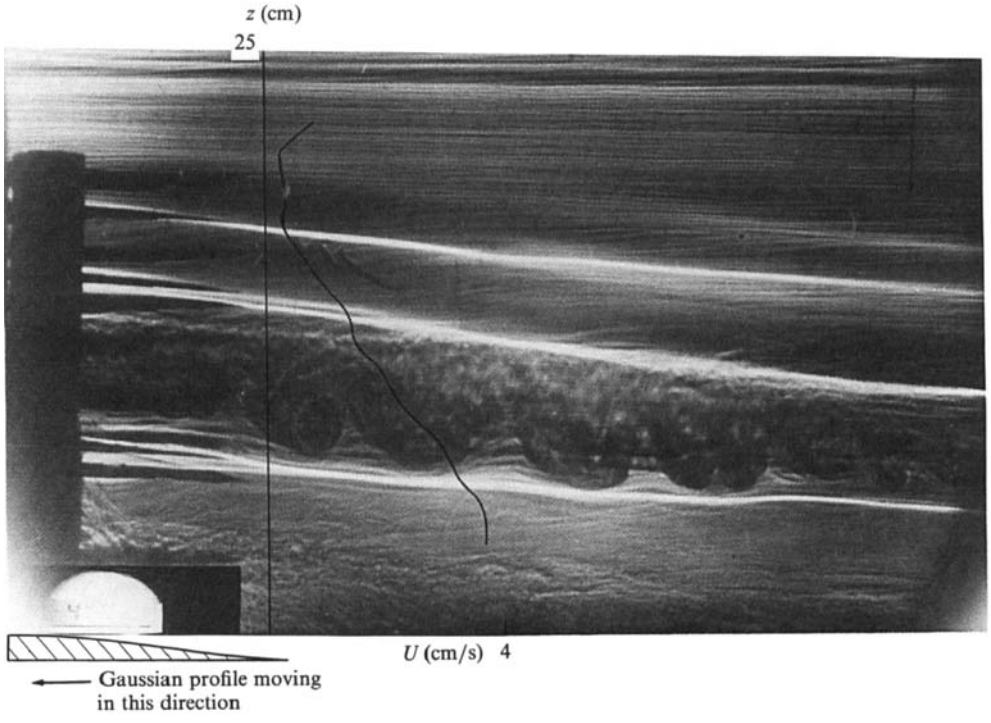

FIGURE 14. Shadowgraph image generated by Gaussian profile 2 for test condition III. Measured velocity profile superimposed on the figure shows that a critical layer did not exist in the flow field.

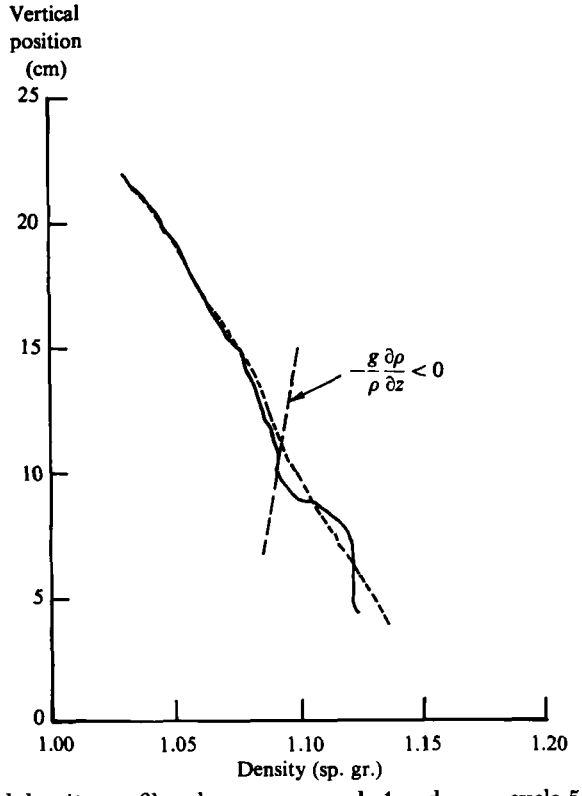

FIGURE 15. Measured density profiles along ----, cycle 1 and ——, cycle 5 for test condition III.

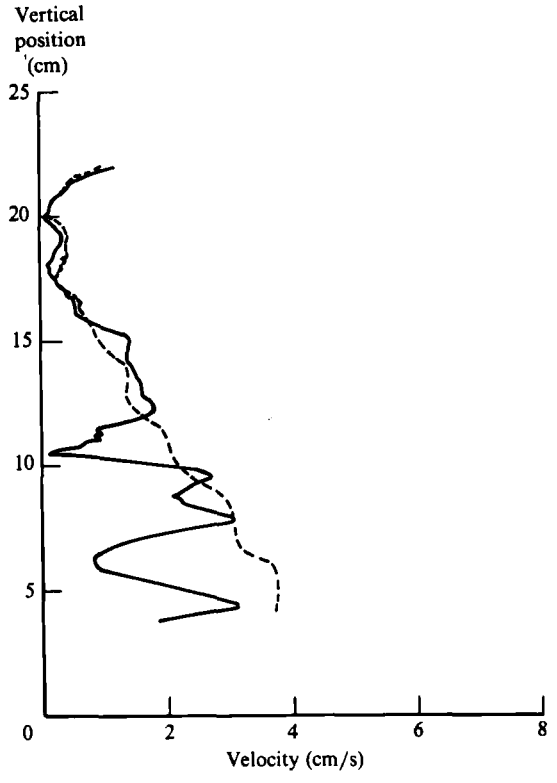

FIGURE 16. Measured velocity profile along ----, cycle 1 and ——, cycle 5 for test condition III.

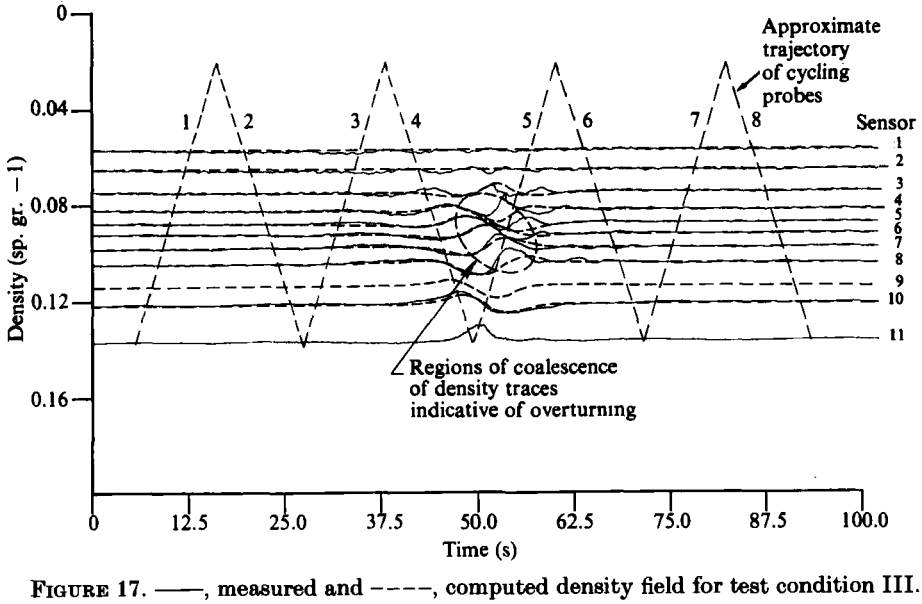

FIGURE 17. ——, measured and ----, computed density field for test condition III.

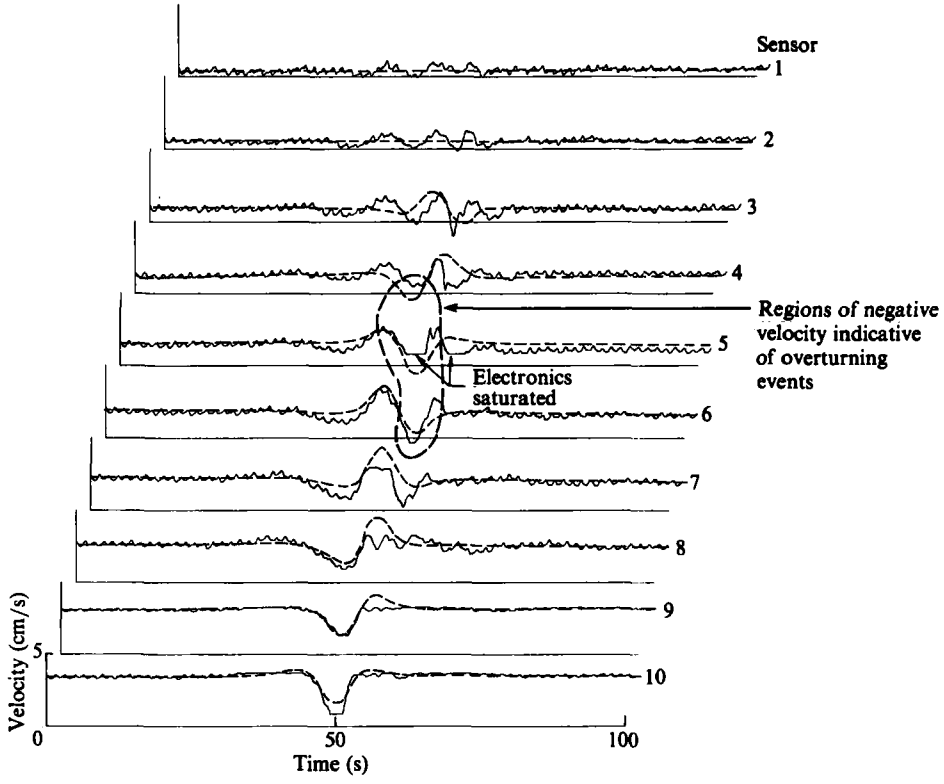

FIGURE 18. ——, measured and – – – –, computed velocity field for test condition III.

towed obstacle but the trailing portion of the wave field exhibits several cycles of a large amplitude disturbance having spatial scales significantly shorter than that of the Gaussian profile. Furthermore, several of the density traces within this area (sensors 3–7) coalesce indicating extended regions of zero or negative density gradient. The location of these higher frequency disturbances and zero density gradient regions closely corresponds with the area where turbulent motions are observed in the shadowgraph visualization. Near the top of the vertical aperture of the array (sensors 1 and 2) the disturbance amplitude diminishes, similar to what is observed for the small-amplitude case of experiment II.

Figure 18 shows the corresponding velocity measurements for this experiment obtained using the hot-film array. In the region where density traces are found to intersect, the velocity traces show evidence of wave-induced zero crossings (sensors 3 and 6; the electronics for sensor 5 saturated during the run but simple extrapolation of the unsaturated measurements suggest a zero crossing for this sensor as well). Again using the Orlanski & Bryan (1969) model, such zero crossings in the velocity data are indicative of waves which have begun to overturn and break as a result of their interaction with the shear flow.

The theoretical density and velocity perturbations for the internal wave field generated by the larger amplitude towed Gaussian profile of experiment III predicted by the wave-action model are shown superimposed on the data in figures 17 and 18. Examining the density field first, it is seen in figure 17 that the cyclic variation of upwelling and downwelling in the forward portion of the wave field (sensors 4–10) is well predicted by the model (to within about 10%). In the trailing portion of the

wave field, however, the agreement between the theoretical predictions and the measurements is quite poor. This is not an unexpected result. In this portion of the wave field, the model predicts regions of zero density gradient which, in a real flow are sites for static instability and turbulence production. Within this region the wave-action model becomes invalid since the dynamics of overturning waves and turbulence production are hardly describable by the model which is based on properties slowly varying in a WKB sense. Thus, in the region of the flow where the model should be valid (i.e. the forward portion of the wave field ahead of the overturning waves) there is good agreement with the measurements. Behind this, in a sense, the model predicts its own obsolescence by predicting regions of negative density gradient where considerations of real flow effects, such as turbulence production from overturning waves, lead to flow fields with significant high-frequency content that would violate the slowly varying assumptions. Above the region of turbulent activity, the model predicts significant attenuation in the internal wave field generated by the towed body. Such attenuation is also noted in the experiments, although the theoretical predictions appear to overpredict the degree of attenuation which is actually observed.

The computed velocity field for this experiment is shown in figure 18. For the lowermost probes in the forward portion of the wave field the observed cyclic variation of fluid deceleration on probe 10 to acceleration on probes 5 and 6 is reproduced by the model within an accuracy of about 10–20 %. Behind this region, the computed velocity for several of the sensors exhibit zero crossings (probes 3–5) in the same region of the flow where negative density gradients are predicted, indicative of wave overturning. Similarly to what is found for the density calculations, when such overturning is predicted from zero crossings in the velocity field the agreement with the measurements is quite poor. Above the region containing overturning waves (sensors 1 and 2) the model predicts significant attenuation in the internal wave-induced contribution to the velocity field. Such a result is observed in the data, although not to the extent predicted by the model.

4.4. *Experiment IV: turbulent critical layer*

For experiment IV, the same Gaussian profile ($a = 0.5$ cm) and towing speed (3.88 cm/s) used in experiment II were employed, but the maximum upper-layer flow velocity was increased to about 5.5 cm/s, such that a critical level existed near the centre of the channel. The ambient Richardson number within the sheared region for this experiment is about 5.0.

Figure 19 shows the shadowgraph image for this experiment. From this visualization one observes that below the critical level there exists a banded region of turbulent fluid inclined at an angle of about 10° to the horizontal. Between this turbulent layer and the critical level the displacement amplitude is seen to diminish, and above the critical level there is no evidence of wave motion correlated with that produced by the towed Gaussian profile.

The measured density perturbations for this experiment, shown in figure 20, exhibit a region of overturning waves in the centre portion of the conductivity probe array consistent with the turbulent region observed in the shadowgraph image. Above the overturning waves (sensors 1–5) the disturbance amplitude diminishes to nearly zero. The computed density field predicts the vertical mode structure of the forward portion of the wave field (downwelling on 9–11 followed by upwelling on sensors 6–8) to an accuracy of about 20 %. In the rear portion of the wave field, the model predicts a negative density gradient region (sensors 6 and 7) in close proximity

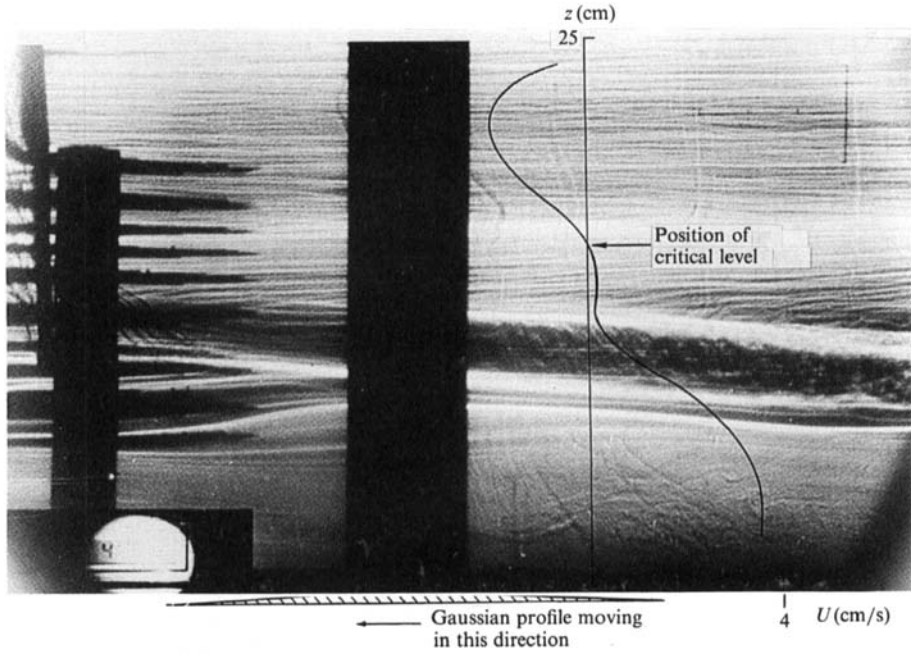

FIGURE 19. Shadowgraph images of wave field generated by Gaussian profile 1 for test condition IV. Measured velocity profile (in coordinate system moving with the towed body) shown superimposed on the photograph.

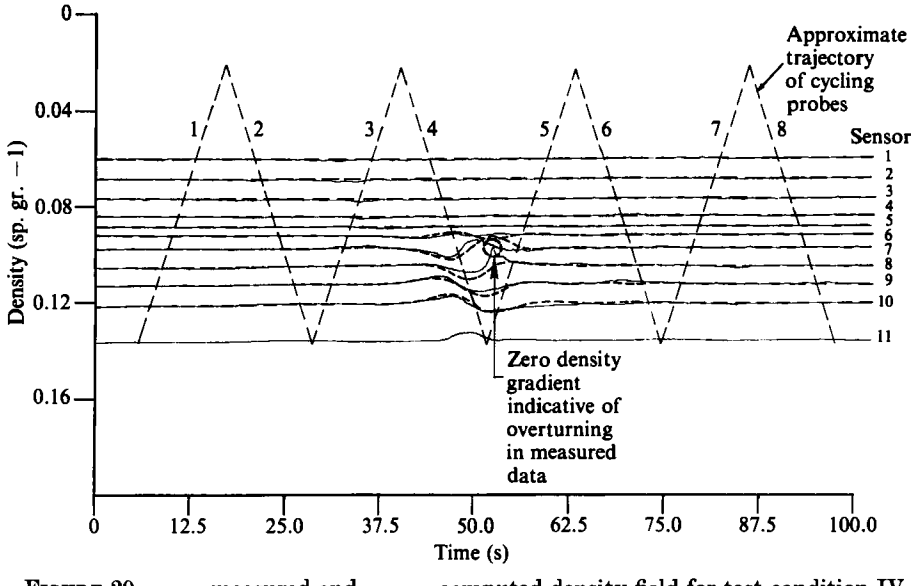

FIGURE 20. ——, measured and – – – –, computed density field for test condition IV.

to where the measured density data show evidence of overturning waves. As expected the agreement with the data in this area is quite poor, owing to the turbulent nature of the flow field in regions of negative density gradient. Above this, the model predictions show the same marked attenuation of the disturbance amplitude that is observed in the measurements.

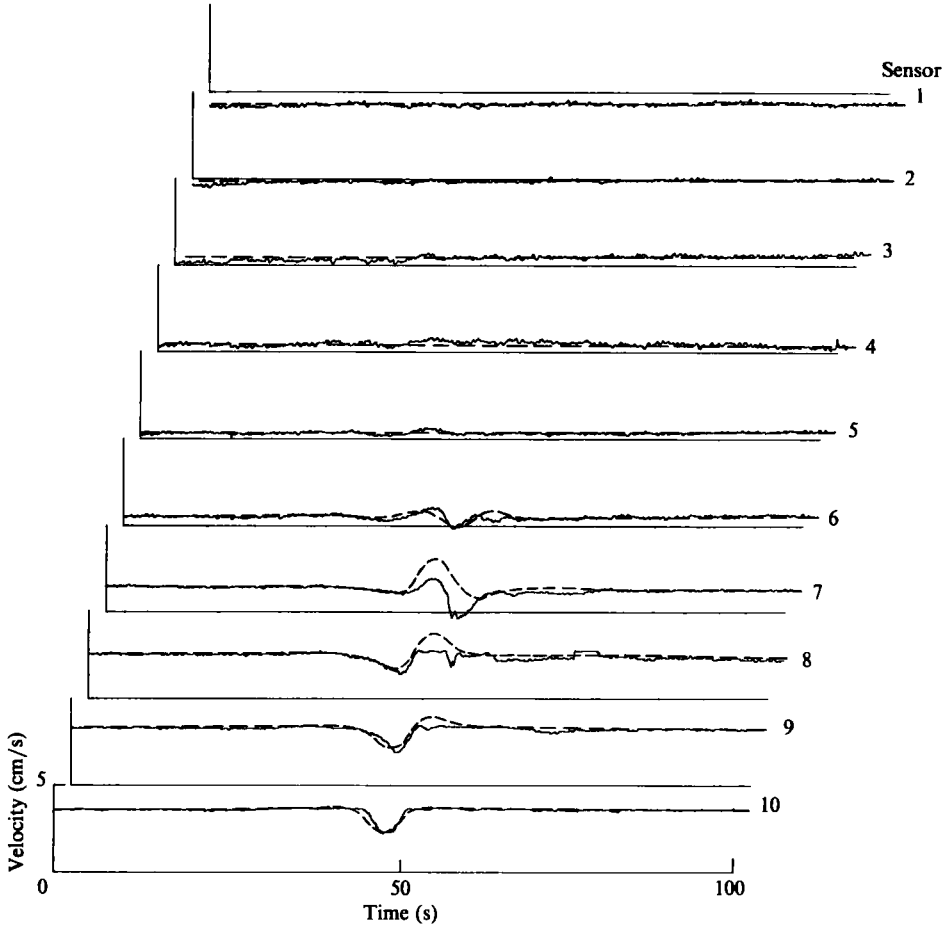

FIGURE 21. ——, measured and – – – –, computed velocity fields for test condition IV.

The corresponding velocity measurements and model predictions are shown in figure 21. Once again, the structure of the forward part of the velocity perturbations are well predicted by the model (to about 5–10 % accuracy), but once a zero crossing in the velocity perturbation occurs (e.g. measured on sensors 6 and 7 and predicted on sensor 6) the model predictions become invalid. Above the region of overturning waves, both the model and the measurements show the same marked attenuation in the disturbance amplitude as the waves approach the critical level.

4.5. *Experiment V: laminar critical layer*

In this last experiment, an example is presented where the initial energy deposition into the wave field by the towed Gaussian-shaped obstacle is sufficiently small that even though a critical level exists the flow is everywhere stable. For this experiment, the 1 cm amplitude Gaussian profile shape was used and the flow conditions were approximately the same as those of experiment II (maximum fluid velocity 3.25 cm/s), but the towing speed of the obstacle was reduced to 2.05 cm/s (compared with 3.88 cm/s for experiment II).

Figure 22 shows the shadowgraph image for this condition. As in experiment IV, the trapping effect that the critical level has upon the vertical propagation of the wave field is observed. Unlike the previous example, however, the critical level is

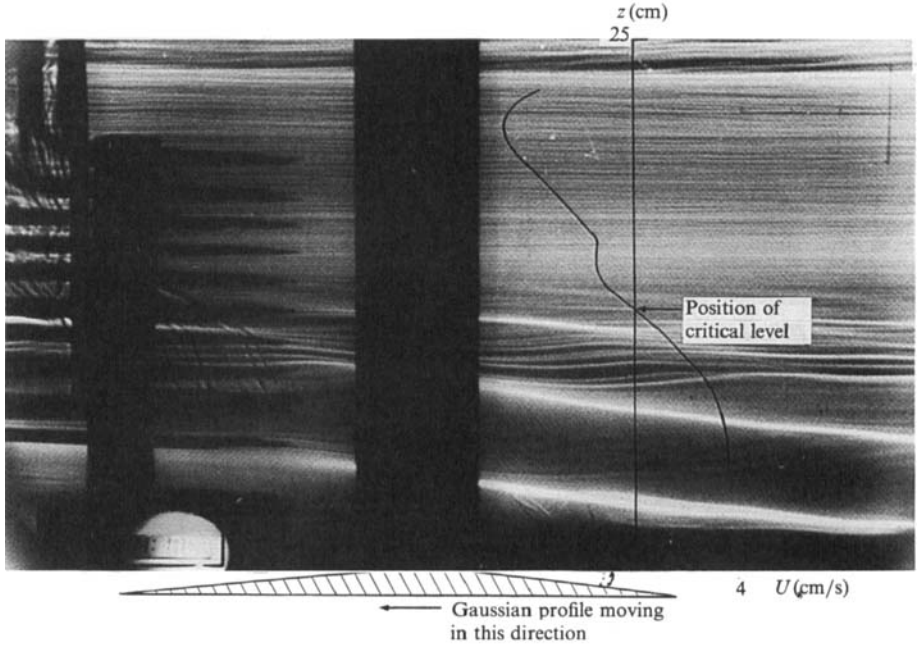

FIGURE 22. Wave field generated by Gaussian profile 2 for test condition V.

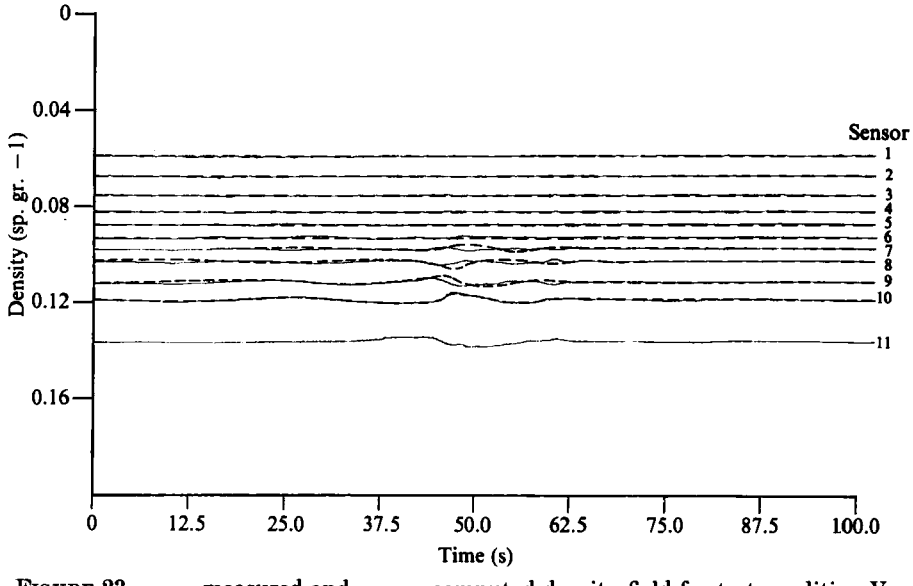

FIGURE 23. ——, measured and – – – –, computed density field for test condition V.

observed to be stable and exhibits no evidence of wave overturning or turbulence generation.

The measured and computed density and velocity fields for this case are shown in figures 23 and 24. All of the results, both measured or computed, support the conclusion that the reduction in the energetics of the initial internal wave field generated by the towed object leads to a stabilization of the flow field in the neighbourhood of the critical level.

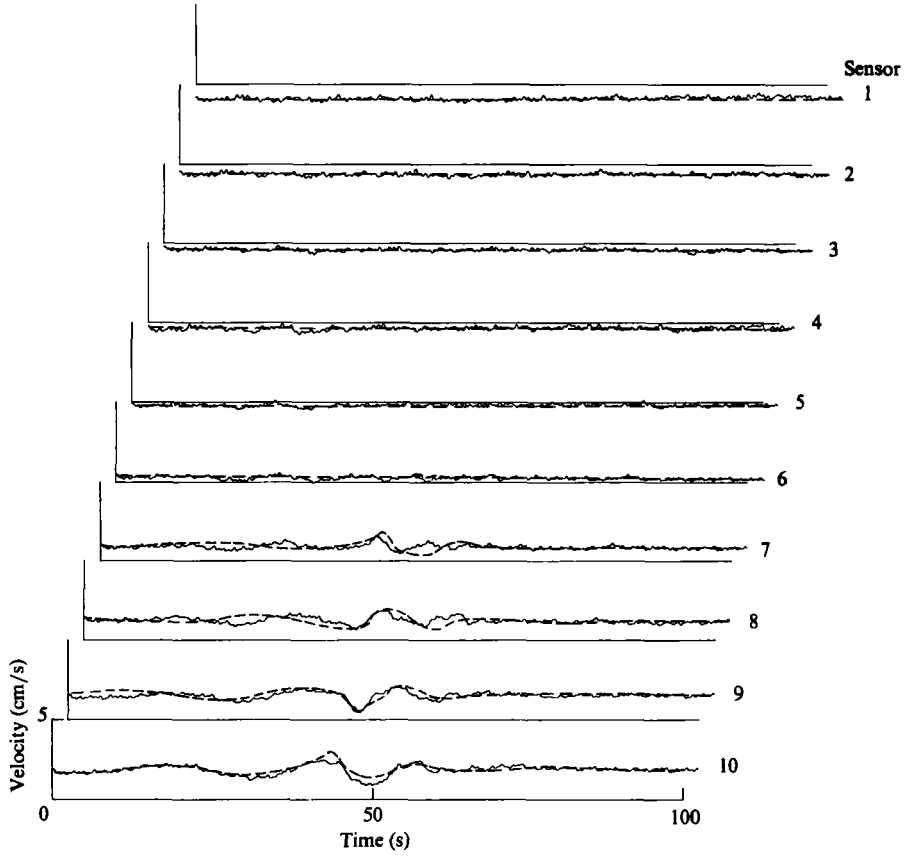

FIGURE 24. ——, measured and – – – –, computed velocity field for test condition V.

5. Summary of results and conclusions

The experimental results presented in the previous section have provided a quantitative description of the interaction of internal waves with a steady shearing motion, and demonstrate the effects of shear on wave overturning, turbulence production, the growth of Kelvin–Helmholtz instabilities, and the suppression of vertical wave propagation by critical level absorption. The experimental results have been compared in a quantitative manner with the predictions of a wave-action analysis, and in general the two compare favourably in regions of the flow where the model assumptions are valid, and poorly where the assumptions are clearly violated.

Typically, in regions below the critical level, on the forward face of the wavetrain agreement to within about 5–10% of the maximum disturbance amplitude is observed between the model and the data. Within this region, the assumptions made in the model appear to be satisfied in the experiment. For example, the slowly varying assumptions inherent in the WKB formulation of the wave-action analysis require that the properties of the medium vary on a scale which is large compared to that of the disturbance. Mied & Dugan (1974) have shown that for this approximation to be valid, $k_z L$ (L being the lengthscale characterizing the mean flow properties) must be greater than about 2. In the present experiment, except in the regions of overturning waves this quantity is always greater than about 10. Similarly

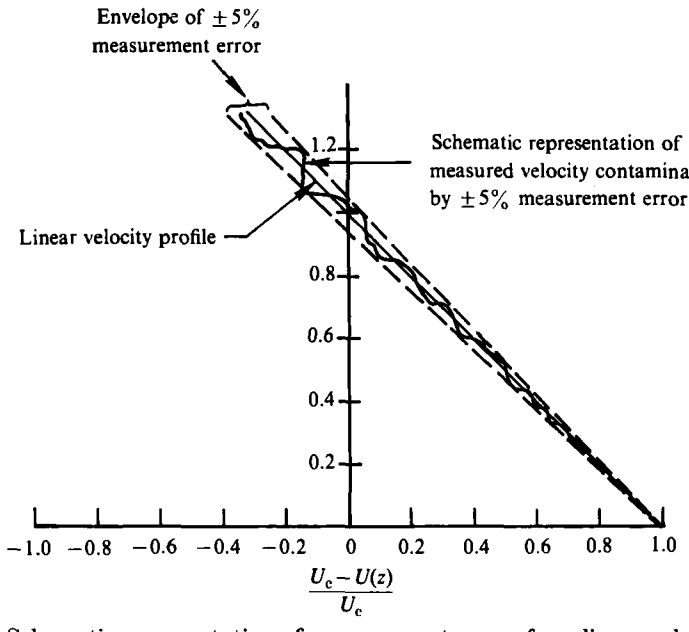

FIGURE 25. Schematic representation of measurement errors for a linear velocity profile. Measurement error assumed to be ±5% of local velocity magnitude.

the model (as formulated in the present paper) assumes the disturbances to be stationary lee waves. For this to be valid, the transients associated with the start-up process of the towing system must have suficient time to radiate many wavelengths away from the source of the internal waves. In Koop (1981) it was determined that the initial start-up transients have negligible effect upon the steady-state wave field when $k_x c_z T$ (T being the time elapsed since the start-up of the towing system) is greater than about 25, and for the present experiment this quantity is typically greater than about 40.

Behind the forward face of the waves, however, in many cases the agreement between the theory and the data is poor. The lack of agreement within this region is believed to be attributable to turbulence produced by the growth of Kelvin–Helmholtz waves or static instabilities due to wave overturning. Such processes violate several of the assumptions inherent in the model, particularly the WKB approximation. It is significant, however, that the model is capable of predicting where such Kelvin–Helmholtz instability or wave overturning might exist in the flow. The calculations for the test condition of figure 9, for example, show that the wave-induced contribution to the Richardson-number distribution produces localized regions where the Richardson number is below the critical value of 0.25 necessary for the growth of Kelvin–Helmholtz instability. For the test conditions of figures 7, 14, and 19, the calculations predicted regions of overturning waves where turbulence should be expected (and is observed), and predicted no such overturning regions for the test conditions of figures 5 and 22 (which is also consistent with the observations).

The comparison between the measurements and the model also showed that as the waves get very close to the critical level, the agreement gets noticeably poorer [cf. figures 12 (sensor 2), 13 (sensor 2), 17 (sensor 3), and 18 (sensors 2 and 3)]. This is possibly due to inaccuracy near the critical level of the velocity profile used in the calculations. In this region small changes in velocity have profound effects upon the predicted values of disturbance amplitude and phase. As an example of how such

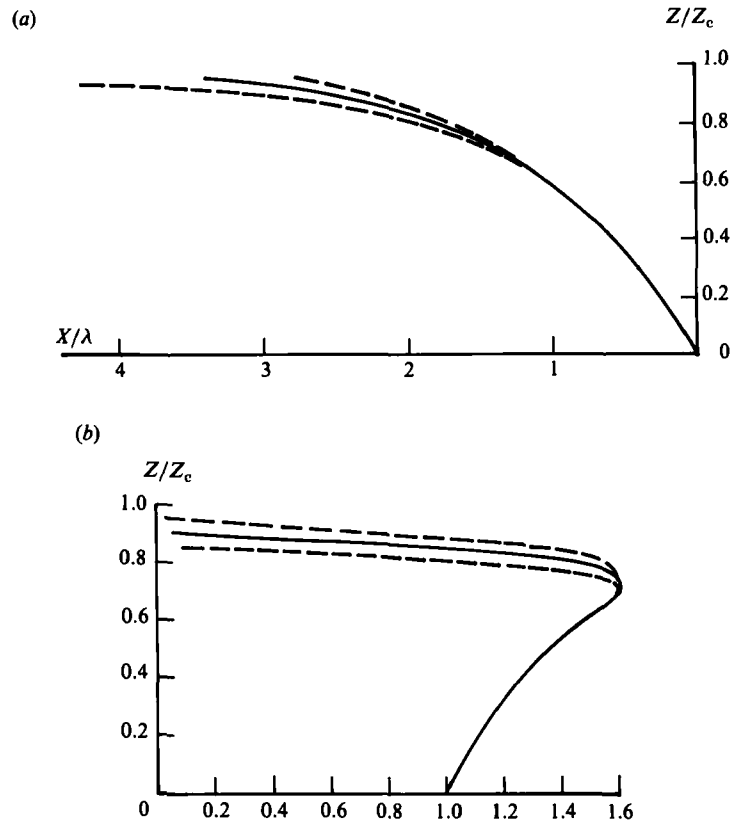

FIGURE 26. Effect of velocity measurement errors on computed phase and amplitude profiles. (*a*) Disturbance phase distribution. (*b*) Disturbance amplitude distribution. ——, calculation for linear velocity profile; – – – –, calculation assuming $\pm 5\%$ measurement error.

measurement error can affect the predicted wave field, consider a shear flow (shown schematically in figure 25) which is linear with depth but can only be measured to an experimental accuracy of (say) $\pm 5\%$, a value not unreasonable for the present apparatus. Using the model discussed in §2, the envelope of uncertainty in predicted amplitude and phase for this degree of experimental inaccuracy is shown in figure 26. The effect of measurement error on the disturbance phase predicted by the model is shown in figure 26(*a*). Below about $z/z_c = 0.75$ the effect of velocity measurement error produces phase errors less than 10% of the disturbance wavelength. Above this point, however, the phase errors grow rapidly with errors as large as two wavelengths or more being observed at $z/z_c = 0.95$. Such phase discrepancies between the theory and the data are evident in figure 13, sensor 2, and figure 18, sensors 3 and 4. The corresponding effect on wave amplitude is shown in figure 26(*b*). Here, once again dramatic effects of measurement error on the magnitude of the wave amplitude are observed close to the critical level, above about $z/z_c = 0.75$, which are consistent with amplitude discrepancies between the theory and the data seen in figure 18 sensors 1 and 2. Thus, for detailed quantitative agreement between predictions and experimental data in regions very close to the critical level extremely accurate measurements of the velocity profile are required. In addition to stringent tolerances on experimental measurement accuracy, it may also be necessary to use in the wave-action model mean velocity measurements made within the wavefield (as

opposed to far upstream of the body). In this manner one could account for modifications of the mean flow by nonlinear interactions between the internal waves and the shear.

This work was supported by the Applied Physics Laboratory of The Johns Hopkins University under contract number APL/JHU 601390, and this support is gratefully acknowledged. The authors also would like to acknowledge the valuable assistance of Mr Dewey Rowland and his assistant Dr Hoy Yo who were responsible for the design and fabrication of much of the experimental apparatus.

Appendix A

In Koop (1981), a simple criterion was presented which predicted the occurrence or non-occurrence of a convective instability in the neighbourhood of a critical layer. Approximating the velocity and density profiles by straight-line segments with $z = 0$ defining the location of the critical level, the criterion for instability involves finding the vertical position z_c in the flow where the density gradient is locally zero. This position is governed by the expression

$$z_c \exp[\phi(z_c)] = \left(\frac{Ri^{\frac{1}{2}} k_{z_0} w_0^2}{U_z^2 k_x^2}\right)^{\frac{1}{3}}, \tag{A 1}$$

$$\phi(z_c) = \frac{1}{9}\frac{Ri^{\frac{3}{2}}}{R_\nu}\left[\frac{1}{(z_c/H_1)^3} - 1\right],$$

$$R_\nu = \frac{k_x C^3}{\nu U_z^2}, \quad H_1 = \frac{C}{U_z},$$

where

Ri = ambient Richardson number,
k_x = horizontal wavenumber of incident wave,
w_0 = maximum vertical velocity induced by incident wave,
U_z = ambient velocity gradient in sheared region,
C = wave phase speed,
ν = kinematic viscosity,
k_{z_0} = vertical wavenumber of incident wave,
$\approx N/C$,
N = Brunt–Väisälä frequency.

If conditions are such that a value of z_c does not exist for which (A 1) is satisfied, then a convective instability does not occur, and the critical layer is predicted to be stabilized by viscous stresses.

For the experimental test conditions of figure 5,

$$Ri \approx 50,$$
$$k_x = 0.55 \text{ cm},$$
$$N \approx 2.5/\text{s},$$
$$C = 2.5 \text{ cm/s},$$
$$U_z \approx 0.35/\text{s},$$
$$w_0 \approx 0.31 \text{ cm/s},$$
$$\nu = 0.01 \text{ cm}^2/\text{s}.$$

Applying the viscous stability criterion of (A 1) for this set of test conditions, one finds that $z_c \exp[\phi(z_c)]$ is always greater than $[Ri^{\frac{1}{2}} k_{z_0} w_0^2/U_z^2 k_x^2]^{\frac{1}{3}}$ for all values of z_c.

Hence the critical layer is predicted to be stable with respect to convective overturning, consistent with the photograph of figure 5.

For the experiment depicted in figure 7,

$$\begin{aligned} Ri &\approx 36, \\ k_x &= 0.42/\text{cm}, \\ N &\approx 2.0/\text{s}, \\ C &= 3.46\ \text{cm/s}, \\ U_z &\approx 0.33/\text{s}, \\ w_0 &\approx 0.64\ \text{cm/s}, \\ \nu &= 0.01\ \text{cm}^2/\text{s}. \end{aligned}$$

For these conditions, one finds that at a position approximately 4 cm below the critical level, (A 1) is satisfied, thus predicting the onset of convective overturning. This result is quite consistent with the photograph of figure 7.

REFERENCES

Bell, T. 1975 Topographically generated internal waves in the open ocean. *J. Geophys. Res.* **80**, 320.

Bretherton, F. 1966 The propagation of groups of internal gravity waves in a shear flow. *Q. J. R. Met. Soc.* A **92**, 466.

Broutman, D. 1982 The interaction of short wavelength internal waves with background current. Ph.D. dissertation, Department of Oceanography, University of California, San Diego.

Grimshaw, R. 1974 Internal gravity waves in a slowly-varying dissipative medium. *Geophys. Fluid Dyn.* **6**, 131.

Grimshaw, R. 1975 Nonlinear internal gravity waves and their interaction with the mean wind. *J. Atmos. Sci.* **32**, 1779–1793.

Koop, G. 1981 A preliminary investigation of the interaction of internal gravity waves with a steady shearing motion. *J. Fluid Mech.* **113**, 347–386.

Koop, G. & Browand, F. 1979 Instability and turbulence in a stratified fluid with shear. *J. Fluid Mech.* **93**, 135–159.

Mied, R. & Dugan, J. 1974 Internal gravity wave reflection by a layered density anomaly. *J. Phys. Oceanogr.* **4**, 493–498.

Munk, W. 1980 Internal waves and small scale processes, in *Evolution of Physical Oceanography*, pp. 264–291, MIT Press.

Orlanski, I. & Bryan, K. 1969 On the formation of the thermocline step structure by large-amplitude internal gravity waves. *J. Geophys. Res.* **74**, 6975.

Thorpe, S. 1981 An experimental study of critical layers. *J. Fluid Mech.* **103**, 321–344.